Advanced Powder Technology 33 (2022) 103590

Contents lists available at ScienceDirect

Advanced Powder Technology

journal homepage: www.elsevier.com/locate/apt

A coarse-grained parcel method for heat and mass transfer simulations of spray coating processes

Stefan Madlmeir [a,*], Stefan Radl [b]

[a] Research Center Pharmaceutical Engineering GmbH, Graz, Austria
[b] Institute of Process and Particle Engineering, Graz University of Technology, Austria

ARTICLE INFO

Article history:
Received 8 November 2021
Received in revised form 7 March 2022
Accepted 20 April 2022

Keywords:
Coarse-graining
CFD-DEM
Heat and mass transfer
Spray coating
Fluidized bed

ABSTRACT

The Discrete Element Method (DEM) is commonly used for modeling the flow of particulate materials. Unfortunately, such detailed simulations are computationally very demanding, restricting its use for industrially-scaled processes. The number of particles in a simulation can be reduced by introducing parcels (i.e., "coarse graining"), which – in essence – relies on the increase of the particle diameter for interaction calculations. However, sophisticated models are necessary to preserve the original behavior of the material when using such an approach. Our present contribution extends available coarse-graining concepts by introducing models for (i) particle–fluid mass transfer and (ii) the deposition rate of spray droplets on particles. Our mass transfer model is based on an existing model for heat transfer. For the spray deposition model, we introduce an effective particle diameter to compute the correct amount of droplets that impact particles. We show that these models can be used with confidence up to a coarse-graining level of 5, which we demonstrate for a simple-shaped fluidized bed. The models proposed by us are critical for detailed simulations of spray coating processes since they enable precise particle-droplet-air interaction modeling at low computational cost.

1. Introduction

With increasing computational power, numerical simulations for modeling granular matter become more and more relevant. One prominent tool is the Discrete Element Method (DEM), which is used to analyze, design and optimize various processes in many industries, e.g., geomechanics [1–3], food [4,5] or pharmaceutical industry [6–11]. DEM can be coupled to Computational Fluid Dynamics (CFD) to model multiphase problems like pneumatic conveying [12], iron ore reduction [13], particle coating [14,15], or fluidized bed processes [16,17]. Since fluid-particle interactions have a major effect on the particle trajectories in these systems, several groups evaluated the effects of different drag laws on the particle behavior [18–21].

Recently, the CFD-DEM method has been extended to include models for droplet deposition, so that coating and granulation processes can be studied in a higher level of detail [22–25]. For this purpose, various spray models have been used in DEM simulations. The most common are the pre-defined spray zone approach [19,24], the ray-tracing method [26,27], the discrete droplet method [28,29] and an Eulerian deposition method [30]. Although all of these models could be applied "inline" (i.e., during a multiphysics simulation), or during post-processing, an inline spray model is necessary if simultaneous momentum, heat and mass transfer should be modeled. Models for heat transfer usually include conductive and convective transport [31,32], but also heat generation due to chemical reactions [13,33] or radiative heat transfer [34,35] can be considered. With the recent incorporation of drying models [28,30,36,37], all major physical phenomena relevant for the simulation of coating processes are covered within the CFD-DEM approach.

Such high-fidelity CFD-DEM simulations – once validated with experimental data – are an extremely powerful tool to analyze, design, and trouble-shoot particle processes that suffer from limited instrumental access. However, thorough validation of the numerical approach is non-trivial as it requires sophisticated measurements. Van Buijtenen [38] extracted particle velocity fields using particle image velocimetry and positron emission particle tracking (PEPT) methods. In addition to particle velocity, PEPT was used by Li et al. [39] to measure cycle times and residence times in a Wurster coating device. The solid volume fraction can be obtained via digital image analysis [40]. Pietsch et al. [19] measured pressure drop fluctuations in the experiments and applied Fast Fourier Transform to obtain frequency plots that can be compared to simulation results. Jiang et al. [41] used color particle

* Corresponding author.
E-mail address: stefan.madlmeir@rcpe.at (S. Madlmeir).

https://doi.org/10.1016/j.apt.2022.103590
0921-8831/

tracking velocimetry to calculate the mixing index in a polydisperse pseudo-2D fluidized bed and showed that drag laws developed for monodisperse particles require modification, if they should be applied to polydisperse systems. Patil et al. [42] used visual and infrared cameras to obtain particle volume fraction, velocity and temperature distributions in a pseudo-2D bed, which is especially useful to validate heat transfer models. Trogrlic et al. [43] placed several temperature and humidity sensors inside a Wurster coater to validate a CFD-DEM approach that includes models for heat and mass transfer. In addition to temperature sensors, Madlmeir et al. [37] validated their simulations by evaluating the coating yield in a Wurster coating process using quantitative nuclear magnetic resonance. The above-mentioned studies prove that CFD-DEM is a suitable tool for precise modeling of coating processes.

Several factors boost the utilization of high-fidelity numerical simulations in process design and optimization: (i) detailed mechanistic models allow truly predictive simulations, critically reducing the number of expensive experimental trials; (ii) extreme geometrical variations can be investigated without expensive physical prototyping; (iii) access to physical quantities that are not measurable, e.g., the temperature of individual particles; and (iv) observation of simultaneously occurring phenomena, e.g., convective and conductive heat transfer rates [32]. However, there still exist limitations which prevent a widespread use of these high-fidelity simulation tools: (i) the variety and complexity of available methods and models requires expert users, who decide, which method is most suitable and which models are required for a specific problem. (ii) Simulation setup, model calibration and validation are often time-consuming tasks that usually have to be accompanied by experiments [44,45]. (iii) Furthermore, the high computational effort for numerically solving the model equations limits the temporal and spatial scale that can be simulated. Nowadays, only seconds to minutes of lab-scale particulate systems can be modelled in high detail - for longer process times or industrially-sized equipment, simplified, multi-scale, or reduced order models are indispensable [23,46,47].

To keep the computational effort within the realms of possibility, two major approaches for reducing the number of particles are common: (i) using a small domain size or (ii) coarse graining. A small simulation domain can be realized by looking only into relevant sections of a device ([30]), utilizing lab-scaled equipment ([28,42]) or taking advantage of symmetries ([22,47]). However, if production-scaled processes should be replicated, the most promising way is the use of a coarse-graining approach [48]. In coarse-graining, the computational effort in DEM-based simulations is reduced by increasing the particle diameter, as this reduces the number of particles to be tracked. To obtain a correct result, simulation parameters or particle properties have to be adjusted. In DEM simulations this is usually achieved with the coarse-grained parcel method (CGPM) [49,50]. For CFD-DEM simulations, similarity models are also available [40,51,52]. In this method, the parameters are adapted so that dimensionless numbers, such as Archimedes and Reynolds number, remain constant. However, these similarity models are only applicable to systems, in which the particle motion is mainly caused by fluid forces, while energy dissipation during particle collisions plays only a minor role [40].

In CGPM, several primary particles are lumped together into a single coarse-grained particle, which is called a parcel. The physical properties of all primary particles represented by a parcel are identical (i.e., they have the same diameter, density, etc.). The density of the parcel is typically chosen to be identical to that of the primary particles, and the mass of the parcel equals the sum of the masses of the primary particles. Hence, the number of parcels that need to be tracked is proportional to α^{-3}, where the coarse-graining level $\alpha = \frac{d_{p,CGP}}{d_{p,O}}$ is defined as the ratio of the parcel diameter $d_{p,CGP}$ and the original particle diameter $d_{p,O}$. By modifying the DEM parameters of parcels, the results of the coarse-grained simulation can successfully represent the real system. In recent years, several studies about DEM coarse-graining models were published, all focusing on predicting the flow (i.e., velocity and position) of a granular material. Specifically, for particle–particle and particle–wall collisions, two main approaches for scaling the contact parameters are used: (i) constant kinetic energy [49] and (ii) constant dimensionless overlap [50]. In both cases, the rebound velocity after contact is the same as for the primary particles. While the duration of the collision is matched only with the first approach, longer collision time allows for an increased simulation time step in the second approach, which further reduces the computation time. Recently, coarse-graining models were extended to account for cohesion and liquid-bridge models [53,54]. Other studies investigated coarse-graining approaches for polydisperse systems [55,56]. Queteschiner et al. [57] proposed a multi-level approach, in which the coarse-graining level is adjusted dynamically in certain regions of the simulation domain. When particle coarse-graining is applied in CFD-DEM simulations, the drag closure has to be adjusted for a correct prediction of fluid-particle forces. This can be achieved by evaluating the drag force for a primary particle and multiplying it with the number of particles per parcel (i.e., α^3) [58]. Similarly, Lu et al. [59] proposed a model for fluid-parcel heat transfer by calculating the heat transfer rate of a primary particle, and then scale it with α^3.

The aforementioned models are thoroughly discussed in literature and are useful to model many industrial processes [19,60,61]. However, after consulting a recent review [48], we identified a gap in knowledge when simulating coating processes: currently, no CGPM-based models for particle drying (i.e., vapor mass transfer rates) and spray deposition (i.e., droplet deposition rates) are available in the open literature. Thus, in our present contribution we close this gap by presenting and validating coarse-graining models for (i) the evaporation of liquid from the surface of coated particles, as well as (ii) the deposition of spray droplets in a monodisperse particle bed. We will show that the development of the evaporation model is relatively straightforward: one can apply the analogy of heat and mass transfer to the available coarse-graining model for heat transfer that has been recently proposed [59].

The spray deposition model is more involved, as it is required to achieve similar deposition characteristics of droplets into a particle bed: when droplets are sprayed onto a particle bed, droplets typically deposit rather quickly, and only penetrate a layer that has a thickness of a few particle diameters. For monodisperse spherical particles, the normalized thickness of this layer (with the particle diameter being the reference length) depends primarily on the packing fraction and droplet parameters (e.g., size and speed) - the particle diameter has no significant effect on this normalized layer thickness. This means for a coarse-grained simulation that the droplet penetration depth would increase - in essence - by the factor α compared to the original sized simulation. This would deteriorate the performance of the coarse-grained approach, and make droplet deposition modeling for large values of α imprecise. Hence, a coarse-graining model for spray deposition is necessary to achieve a similar penetration depth, and hence spray distribution in the particle bed. Our core idea is to increase the effective diameter of the parcels in our droplet-parcel interaction algorithm to match the behavior in the original DEM-based (non coarse-grained) model. This pragmatic approach can be easily implemented in all existing DEM codes, and leads to the correct amount of droplets depositing on parcels closer to the source of the droplets (e.g., a nozzle). We will show that this effective parcel diameter for droplet-parcel interaction must depend on (i) the

coarse-graining level, and (ii) the particle volume fraction. Based on a model for granular filtration, we have finally developed a semi-empirical correlation for calculating this effective diameter in (CFD-)DEM simulations.

The mass transfer and spray deposition models are validated separately in simulations of packed beds at various coarse-graining levels and packing fractions. Finally, a top-spray coater is simulated to validate the coarse-graining approach in an industrially relevant process, including models for contact forces, drag, particle–fluid heat and mass transfer as well as spray deposition.

2. Methods

In our present study we utilize the commercially available AVL Fire/XPS software framework [18] for performing the CFD-DEM simulations. XPS carries out the DEM simulation via a Graphics Processing Unit (GPU), which enables fast and effective parallel computation of the particle phase. Additionally, this framework separates the physical quantities that are transferred between the CFD and DEM codes from the irregular CFD mesh by introducing a coupling grid, which is a regular mesh that spans the entire simulation domain. A mapping algorithm interpolates the fluid velocity and temperature from the CFD cells to the center of the coupling cells, and subsequently to the particle positions. Vice versa, the particle volume fraction and the fluid-particle interaction terms are calculated in DEM and are transferred to CFD via the coupling grid [18]. Note that there is no restriction on the size of the CFD cells, which would usually be the case for CFD-DEM simulations, as the cell size needs to be larger than the largest particle diameter unless smoothing is applied [62]. Hence, we use the same CFD mesh in all simulations with different coarse graining levels, and only adjust the size of the coupling grid cells: in all our simulations, this coupling grid cell size is set to 2.5 times the parcel diameter in every spatial direction.

In the following section, the governing equations for the CFD-DEM approach are outlined, including the fluid and particle phase, spray modeling and the applied rules for coarse-graining. A detailed description of CFD-DEM in general [63] and the AVL Fire/XPS framework in particular [18,37,43,64] can be found in literature. Here, we focus on the most relevant equations only.

2.1. Flow model

The particle movement is calculated via a simplified version of Newton's equations of motion:

$$\rho_p V_p \frac{d\boldsymbol{v}_p}{dt} = \boldsymbol{f}_c + \rho_p V_p \boldsymbol{g} - V_p \nabla p + \boldsymbol{f}_d \tag{1}$$

$$I_p \frac{d\boldsymbol{\omega}_p}{dt} = \boldsymbol{M}_p \tag{2}$$

where ρ_p is the particle density, V_p is the particle volume, $\boldsymbol{v}_p$ is the particle velocity, $\boldsymbol{f}_c$ is the sum of all particle–particle and particle–wall contact forces, $\boldsymbol{g}$ is the gravitational acceleration, ∇p is the (resolved) pressure gradient obtained from the CFD simulation, and $\boldsymbol{f}_d$ is the drag force. I_p is the moment of inertia, $\boldsymbol{\omega}_p$ is the angular particle velocity and $\boldsymbol{M}_p$ is the total torque acting on the particle resulting from contacts with other particles or walls. Eqs. (1) and (2) assume a fixed particle mass, insignificant momentum transfer upon droplet-particle impact (the ratio of droplet momentum to particle momentum is $\mathcal{O}(10^{-4})$), as well as spherical particles. These assumptions are justified in most typical coating applications, at least the ones found in typical pharmaceutical applications.

To calculate the contact forces, a linear spring-dashpot model described by Forgber et al. [64] is applied. We neglected liquid bridge forces in our model, which can be justified with the low liquid hold-up present in the system. By applying the coarse-graining model of Sakai and Koshizuka [49], which is based on constant kinetic energy, the contact forces are scaled with α^3

$$\boldsymbol{f}_{c,CGP} = \alpha^3 \boldsymbol{f}_{c,O} \tag{3}$$

where the indices "*CGP*" and "*O*" denote coarse-grained particle and original sized particle, respectively.

The drag force can be calculated as.

$$\boldsymbol{f}_d = \beta V_p (\boldsymbol{v}_f - \boldsymbol{v}_p) \tag{4}$$

where β is the drag coefficient and $\boldsymbol{v}_f$ is the fluid velocity. The model of Beetstra et al. [65] is used to evaluate the drag coefficient. As discussed earlier, the drag force in a coarse-grained simulation is determined for a primary particle and then scaled accordingly, [49,66], leading to.

$$\boldsymbol{f}_{d,CGP} = \alpha^3 \boldsymbol{f}_{d,O} \tag{5}$$

The fluid phase is modeled with the volume-averaged Navier-Stokes equations, given as.

$$\frac{\partial}{\partial t}\left(\phi_f \rho_f\right) + \nabla \cdot \left(\phi_f \rho_f \boldsymbol{v}_f\right) = 0 \tag{6}$$

$$\frac{\partial}{\partial t}\left(\phi_f \rho_f \boldsymbol{v}_f\right) + \nabla \cdot \left(\phi_f \rho_f \boldsymbol{v}_f \boldsymbol{v}_f\right) = -\nabla \cdot \left(\phi_f \tau_f\right) - \phi_f \nabla p + \phi_f \rho_f \boldsymbol{g} - \frac{1}{V_{cell}} \sum\nolimits_n \beta V_{p,n} (\boldsymbol{v}_f - \boldsymbol{v}_{p,n}) \tag{7}$$

where ϕ_f is the local fluid volume fraction, ρ_f is the fluid density (constant fluid density was used in the simulations) and $\boldsymbol{v}_f$ is the fluid velocity vector. τ_f is the deviatoric fluid stress tensor, p is the fluid pressure, and $\boldsymbol{g}$ is the gravitational acceleration. The last term in Eq. (7) accounts for the momentum exchange between the particle and the fluid phase. In this term, V_{cell} is the volume of the (fluid) grid cell, and β is the drag coefficient. Furthermore, $V_{p,n}$ and $\boldsymbol{v}_{p,n}$ denote the volume and velocity of parcel n located in a specific (fluid) grid cell, respectively.

2.2. Heat and mass transfer model

We assume that the temperature gradient inside a particle is negligible, i.e., the whole particle has the same temperature. Consequently, we follow the approach of Kolar et al. [67] in assuming that deposited liquid has the same temperature as its carrier particle (i.e., infinitely fast heat transfer) and thus simplifying the drying model significantly. Otherwise, heat transfer from the gas phase and the particle to the deposited droplet would have to be considered along with the latent heat of evaporation [68]. Additionally, we neglect the mass-change of the particle, as well as conductive heat transfer – both phenomena are typically unimportant in the flow regimes we study (i.e., coating in a fluidized bed) and also not a focal part of our present study. Furthermore, we did not consider evaporation of spray droplets before their deposition on a particle surface. For coarse-graining of conductive heat transfer rates, the interested reader is referred to the excellent study of Lu et al. [59]. With these simplifications the enthalpy change of a particle calculates as.

$$\rho_p V_p c_p \frac{dT_p}{dt} = \dot{Q}_{f,p} + \dot{H}_v \tag{8}$$

where c_p is the specific heat capacity of the particle and T_p is the particle temperature. $\dot{Q}_{f,p}$ is the heat transfer rate between the fluid and the particle, and $\dot{H}_v$ is a latent heating (or cooling) rate. The fluid-particle heat transfer rate is calculated as.

$$\dot{Q}_{f,p} = hA_p(T_f - T_p) \tag{9}$$

with h being the heat transfer coefficient, A_p being the surface area of the particle and T_f being the fluid temperature. For the heat transfer coefficient, the correlation of Gunn [69] is used. As previously proposed [59], the single-particle heat transfer rate is calculated for a primary particle and scaled with the number of particles per parcel:

$$\dot{Q}_{f,p,CPG} = \alpha^3 \dot{Q}_{f,p,O} \tag{10}$$

The latent heating rate can be calculated as.

$$\dot{H}_v = -\dot{m}_v \Delta H_v \tag{11}$$

where $\dot{m}_v$ is the evaporation rate, and ΔH_v is the specific latent heat of evaporation. The closure used to calculate the evaporation rate is.

$$\dot{m}_v = \pi a_w d_p \rho_v D Sh \ln(1 + B_M) \tag{12}$$

where a_w is the wet-to-total particle surface area ratio, d_p is the diameter of the particle, ρ_v is the vapor density, D is the diffusion coefficient of the vapor in the ambient fluid (i.e., air), Sh is the Sherwood number and B_M is the Spalding mass transfer number, which is defined as.

$$B_M = \frac{w_{v,s} - w_{v,\infty}}{1 - w_{v,s}} \tag{13}$$

where $w_{v,s}$ and $w_{v,\infty}$ are the vapor mass fractions on the surface of the particle and in the bulk, respectively. The surface vapor mass fraction was calculated using the Antoine equation. The droplet spreading model of Asai et al. [70] and the surface coverage model of Kariuki et al. [71] are applied to calculate the wet-to-total particle surface area ratio a_w. The surface area of a parcel is calculated as the sum of the areas of its primary particles. By using the model of Kariuki et al. [71], we assume that particle rotation is sufficiently fast to lead to a random distribution of droplet deposition locations on each particle.

A detailed description of the evaporation model and how to obtain its parameters is provided in Madlmeir et al. [37]. Similar to the heat transfer model, the evaporation rate in the coarse-grained system is calculated for a single primary particle and scaled up:

$$\dot{m}_{v,CGP} = \alpha^3 \dot{m}_{v,O} \tag{14}$$

The energy balance of the fluid phase is given as.

$$\phi_f \rho_f c_{p,f} \frac{\partial T_f}{\partial t} + \nabla \cdot \left(\phi_f \rho_f \boldsymbol{v}_f c_{p,f} T_f\right) - \nabla \cdot \left(\lambda_{eff} \nabla (\phi_f T_f)\right) = -\frac{1}{V_{cell}} \sum\nolimits_n \dot{Q}_{f,p,n} \tag{15}$$

where $c_{p,f}$ is the specific heat capacity of the fluid, and λ_{eff} is the effective thermal conductivity. The term on the right side sums up the fluid-particle heat flux of all particles in the coupling cell with the volume V_{cell}. Note that there is no explicit term that considers evaporative cooling of the fluid phase, since in our model the latent heat contributes to the particle energy balance only (see Eq. (8)). Nevertheless, the fluid cools down indirectly due to fluid-particle heat transfer.

The vapor mass fraction in the fluid phase is determined via the species transport equation:

$$\frac{\partial}{\partial t}\left(w_v \phi_f \rho_f\right) + \nabla \cdot \left(w_v \phi_f \rho_f \boldsymbol{v}_f\right) - \nabla \cdot \left(D_{eff} \nabla \left(w_v \phi_f \rho_f\right)\right) = \sum\nolimits_n \dot{m}_{v,n,i} \tag{16}$$

where w_v is the vapor mass fraction and D_{eff} is the effective diffusion coefficient of vapor in air.

2.3. Spray model

In the present contribution, we utilize an inline ray-tracing method, which proved itself as an valuable alternative to the computationally expensive discrete droplet method [26,43,72]. The principle is quite simple: originating from the spray nozzle, rays are randomly distributed inside a user-defined spray cone, where every ray represents a spray droplet. In discrete time intervals, intersections between rays and particles are detected and a droplet is deposited on the particle that is closest to the nozzle. A ray intersects a particle if the following condition is satisfied:

$$\left(\boldsymbol{x}_p - \boldsymbol{x}_o\right)^2 - \left(\left(\boldsymbol{x}_p - \boldsymbol{x}_o\right) \cdot \boldsymbol{x}_{dir}\right)^2 \leq \left(\frac{d_d}{2} + \frac{d_p}{2}\right)^2 \tag{17}$$

where $\boldsymbol{x}_p$ is the particle position, $\boldsymbol{x}_o$ and $\boldsymbol{x}_{dir}$ are the origin and the unit-length direction vector of the ray; d_d and d_p are the droplet (ray) and particle diameter, respectively. How to modify this "hit detection equation" in case one only has parcel information at hand is not obvious as we discuss next.

The volume fraction of coarse-grained particles is comparable (and theoretically identical) to the one of primary particles in all regions of the simulation domain. As we will show below, this would cause spray droplets to penetrate deeper into the particle bed in case it is coarse grained: the reason is – simply speaking - that the distance between particles linearly increases with the coarse graining level. To avoid this behavior, we need to replace the parcel diameter $d_{p,CGP}$ in the hit detection equation (i.e., Eq. (17)) with a somewhat larger effective diameter $d_{eff,CGP}$ to match the deposition rate of droplets on the original particles with diameter $d_{p,O}$. We propose to calculate this effective diameter $d_{eff,CGP}$ by multiplying the coarse-grained particle diameter $d_{p,CGP}$ with an effective size factor f_r that depends on the local particle volume fraction ϕ_p and the coarse-graining level α:

$$d_{eff,CGP} = f_r(\alpha, \phi_p) d_{p,CGP} = f_r(\alpha, \phi_p) \alpha d_{p,O} \tag{18}$$

In order to lay the foundation for a theoretical model for the effective size factor f_r, we observe that spray droplet deposition in a particle bed is governed by a similar mechanism as granular filtration. Therefore, our coarse-graining model builds on the filter model of Kolakaluri [73], which was previously used for modeling droplet deposition in a spray coating simulation [30]. Specifically, we observe that in a monodisperse packed bed (comparable to a clean-bed filter) that has a filtration coefficient λ, the droplet deposition along the spray direction can be calculated as:

$$\ln\left(\frac{m_x}{m_{in}}\right) = -\lambda x \tag{19}$$

where m_x is the cumulative deposited mass up to the bed depth x and m_{in} is the total spray mass. From Eq. (19) it is evident that the filtration coefficient λ needs to be identical in the original DEM-based and the coarse-grained simulation. The filtration coefficient can be calculated as [73]:

$$\lambda = \frac{3\eta_s \phi_p}{2 d_p} \tag{20}$$

where η_s is the single collector efficiency, ϕ_p is the particle volume fraction and d_p is the particle (or parcel) diameter. The single collector efficiency (which is a function of particle Reynolds number, the droplet Stokes number and the particle volume fraction) should be independent of the coarse-graining parameter α, which can be achieved relatively easily. Once this is guaranteed, it is clear that the effective particle diameter for spray deposition needs to be chosen such that:

$$\frac{\phi_{p,O}}{d_{p,O}} = \frac{\phi_{eff,CGP}}{d_{eff,CGP}} = \frac{\phi_{eff,CGP}}{f_r \alpha d_{p,O}} \tag{21}$$

is ensured. This leads to the conclusion that $\phi_{eff,CGP} = f_r \alpha \phi_{p,O}$, where $\phi_{eff,CGP}$ is the hypothetical volume fraction of the system if the particles would have the (hypothetical) effective diameter. Thus, we need to supply an additional equation for $\phi_{eff,CGP}$ in case particles are enlarged from diameter $d_{p,CGP}$ to diameter $d_{eff,CGP}$ in a fixed volume. Next, we present two analytical scenarios for this:

Analytical scenario 1: Overlap not considered.

For a monodisperse system, the local volume fraction in a grid cell with volume V_{tot} is defined as:

$$\phi_p = \frac{\pi d_p^3 N_p}{6 V_{tot}} \tag{22}$$

where N_p is the number of particles in the cell. If we neglect the fact that parcels will overlap if their diameter is increased to the effective diameter, the effective volume fraction can be calculated as follows:

$$\phi_{eff,CGP} = \frac{\pi d_{eff,CGP}^3 N_{p,CGP}}{6 V_{tot}} \tag{23}$$

When considering that the number of parcels $N_{p,CGP} = \alpha^{-3} N_{p,O}$, and by considering Eqs. (18) and (21)–(23), we arrive at the following equation for the effective size factor:

$$f_r' = \alpha^{0.5} \tag{24}$$

This scenario is rather unrealistic, since in our simulations rays interact with spherical parcels having the scaled diameter $d_{eff,CGP}$, and these parcels do overlap for ϕ_p close to the close-packing limit.

Analytical scenario 2: Overlap considered.

Considering overlapping particles, an alternative relation can be derived (see Appendix A for a detailed derivation):

$$f_r'' = \left(1 - \frac{ln\left(\frac{1 - f_r'' \alpha \phi_p}{1 - \phi_p}\right)}{\phi_p}\right)^{\frac{1}{3}} \tag{25}$$

Note that f_r'' is implicitly defined via Eq. (25), however, only depends on α and the particle volume fraction. Thus, this equation can be solved numerically at the beginning of the simulation, and tabulated for different values of ϕ_p if α is constant. If the volume fraction is evaluated dynamically, as usually done in CFD-DEM simulations, this would prevent solving Eq. (25) numerically for every droplet/ray interaction. Another simple way to overcome the numerical solution of Eq. (25) would be to approximate f_r'' with f_r' in the right side of Eq. (25). Unfortunately, this equation has a mathematical limit originating from the fact that the argument of the logarithm function in Eq. (25) cannot be negative. This implies the following restriction:

$$f_r'' \alpha \phi_p < 1 \tag{26}$$

Semi-Empirical Model.

To avoid the restrictions of the analytical model, we introduce an additional, universally applicable semi-empirical model that extends Eq. (24) by a heuristically chosen correction term that models the effect of the particle volume fraction:

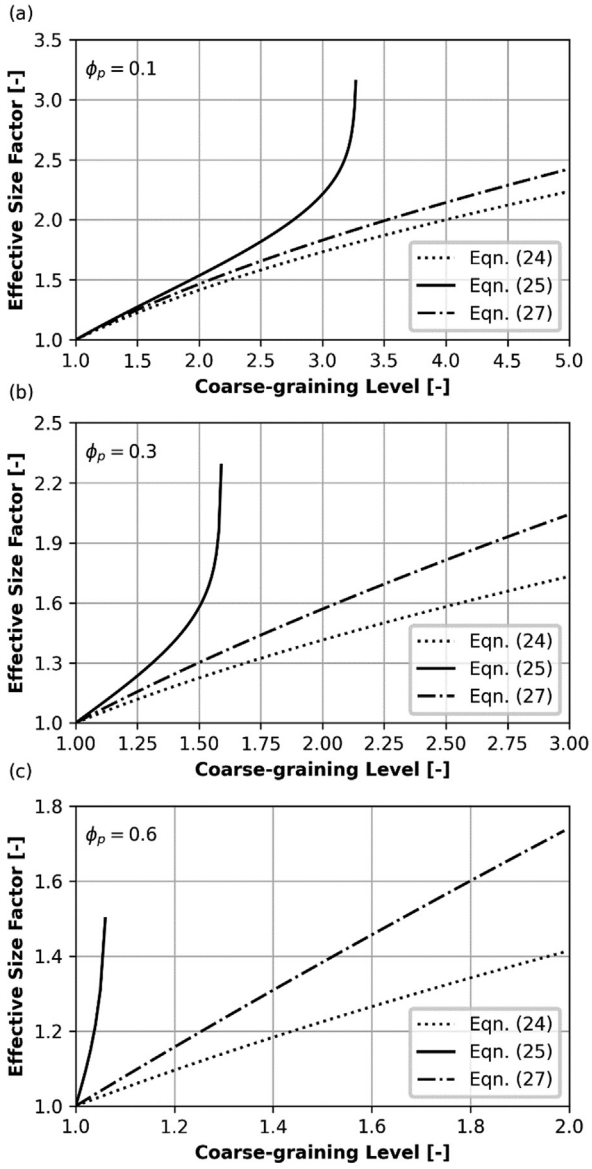

Fig. 1. Comparison of various models for the effective size factor for a particle volume fraction of (a) 0.1, (b) 0.3 and (c) 0.6.

$$f_r = \alpha^{0.5(1+\phi_p)} \tag{27}$$

Fig. 1(a–c) shows a comparison of the different models for the effective size factor for particle volume fractions of 0.1, 0.3 and 0.6. All models satisfy the limiting conditions of (i) $f_r = 1$ at $\alpha = 1$, and (ii) $f_r = \sqrt{\alpha}$ at $\phi_p = 0$. The values obtained with the semi-empirical model (Eq. (27)) are in between those of the analytical scenarios given by Eq. (25) and Eq. (24). While for low volume fractions and coarse-graining levels the models predict a similar effective size factor f_r, the results deviate significantly at high particle volume fractions. Close to the mathematical limit stated in Eq. (26), a steep increase in the factor obtained with Eq. (25) is visible. In this region, the effective volume fraction is already close to unity. Hence, the effective diameter has to increase significantly to obtain a small change in volume fraction. Although Eq. (25) represents the exact analytical solution to account for the diameter enlargement, we observe that this model overestimates the effective size factor: Applying this model to a coarse-grained simulation would lead to a lower spray penetration depth compared to the original-sized case (data not shown). Therefore, we used the

semi-empirical correlation with a lower slope than that of Eq. (25). Furthermore, our semi-empirical model is not limited to the range defined by Eq. (26).

We note in passing that the presented coarse-graining model is not limited to ray-tracing spray methods because it is derived from a fundamental equation for granular filtration: it is expected to work well also for other models that treats droplets as discrete entities, e.g., it is also applicable to the discrete droplet model.

3. Results and discussion

In this section, validation cases for the presented coarse-graining models are investigated. The numerical procedure and coupling routine were extensively validated against experiments in previous work [37,43,64]. Therefore, we refrain from running additional validation experiments, but compare the coarse-grained simulations to the original-sized case. Models for coarse-graining contact and drag forces are already thoroughly examined in literature [55,58,59,74,75], hence we omit discussing these models. Instead, we focus on the new models introduced in our present work. At first, we validate the heat and mass transfer model, followed by the spray deposition model. Finally, all relevant phenomena in a top-spray fluidized bed coater are simulated to investigate the combination of all models in an industrially relevant process. To investigate the limits of the coarse-graining approach, all simulations are carried out with coarse-graining levels of 1 (reference case), 2, 5 and 10.

3.1. Heat and mass transfer model

The performance of the coarse-graining model for heat and mass transfer is evaluated in a CFD-DEM simulation of a static bed containing wetted particles, which are dried by hot air flowing from bottom to top with a velocity of 0.1 m/s. A particle bed was created by randomly placing non-overlapping monodisperse particles in a rectangular box until a particle volume fraction of 0.3 is achieved. To avoid wall effects, only the particle center has to be inside the boundaries, not the whole particle. The particle positions are fixed during the simulation, i.e., all forces acting on the particles and the particle velocities were set to zero. 10 ml of water were uniformly distributed across all particles. The CFD mesh consist of 256,000 cubical cells with an edge length of 2.5 mm. Table 1 contains all relevant material properties and operating conditions, the simulation setup is depicted in Fig. 2.

Fig. 3a shows the mean particle temperature over time for various coarse-graining levels. As the water evaporates from the particle surface, the latent heat of evaporation causes a temperature

Table 1
Material properties and operating conditions for the coarse-graining validation runs.

Property	Unit	Value
Particles		
Diameter	mm	1
Density	kg/m^3	1292
Heat capacity	J/kg/K	1360
Initial temperature	K	333.15
Air		
Inlet temperature	K	333.15
Inlet humidity	–	0
Density	kg/m^3	1.1
Heat capacity	J/kg/K	1007
Thermal conductivity	W/m/K	0.0257
Water		
Density	kg/m^3	997
Heat capacity	J/kg/K	4181
Latent heat	kJ/kg	2427.3
Diffusion coefficient in air	mm^2/s	28

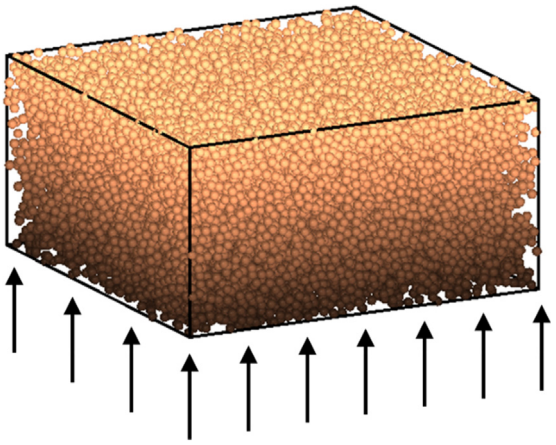

Fig. 2. Simulation setup for the heat and mass transfer simulations. The dimensions of the box are 200 × 200 × 100 mm (LxWxH). The coarse-graining level is 5, the black arrows indicate the drying air flow.

decrease of the fluid and particles. In the reference case, the particles were dry after a simulation time of 15.5 s, and at this point the temperature dropped to 321.88 K. Subsequently the temperature starts to rise again, as the particles are heated by the hot inlet air. An excellent result is observed for a coarse-graining level of 2, for which the temperature at 15.5 s deviates only 0.01 K from the reference case. With increasing coarse-graining level, the deviation in average particle temperature at 15.5 s increases to 0.19 K for $\alpha = 5$, and 0.67 K for $\alpha = 10$. A simulation for $\alpha = 5$ without applying the coarse-graining model for mass transfer given in Eq. (14) results in a deviation of 1.01 K from the reference case. This highlights the importance of applying a scaling rule when running coarse-grained simulations.

The particle temperature distribution after a simulation time of 10 s is shown in Fig. 3b. The mean value of the reference case is 324.88 K and is met closely by the coarse-grained simulations. The maximum deviation occurs at the $\alpha = 10$ case, in which the mean temperature is smaller by 0.15 K. For the $\alpha = 5$ case, the difference is only 0.03 K if the scaling law is used, but 0.65 K without the scaling law. Larger deviations are observed for the median value, which is 2.56 K higher in the $\alpha = 10$ case compared to the reference case. In the coarse-grained simulation with $\alpha = 5$, the median value is 0.91 K closer to the reference case than in the simulation without the scaling law. The spread of the distribution, defined as the difference between the higher and lower value of the whiskers, is 10.78 K for the reference case. The results for $\alpha = 2$ (10.77 K) and $\alpha = 5$ (10.41 K) are very close to the reference case, while significant deviations are observed for $\alpha = 10$ (7.39 K) and the $\alpha = 5$ case when the scaling law is disabled (7.97 K).

Fig. 4 shows the evolution of the global evaporation rate over time. Initially the air is not saturated with vapor, leading to a high vapor concentration gradient, and subsequently to high evaporation rates. With increasing vapor loading, this peak flattens and then the evaporation rate remains almost constant, showing only an insignificant decrease upon the gradual temperature decrease in the system. This stage is followed by a rapid decline of the evaporation rate when the liquid water content drops. The maximum evaporation rate in the reference case is 0.87 g/s, compared to 1.22 g/s for a coarse-graining level of 10. We found that the reason for this significant difference is the coarser coupling grid: as described in section 2, the coupling grid is scaled with the coarse-graining level. When running the static bed simulation with primary particles ($\alpha = 1$) and using the coarse coupling grid (as would be used for $\alpha = 10$), the peak evaporation rate is of 1.18 g/s. Since this value is just 3.3 % smaller than the 1.22 g/s for

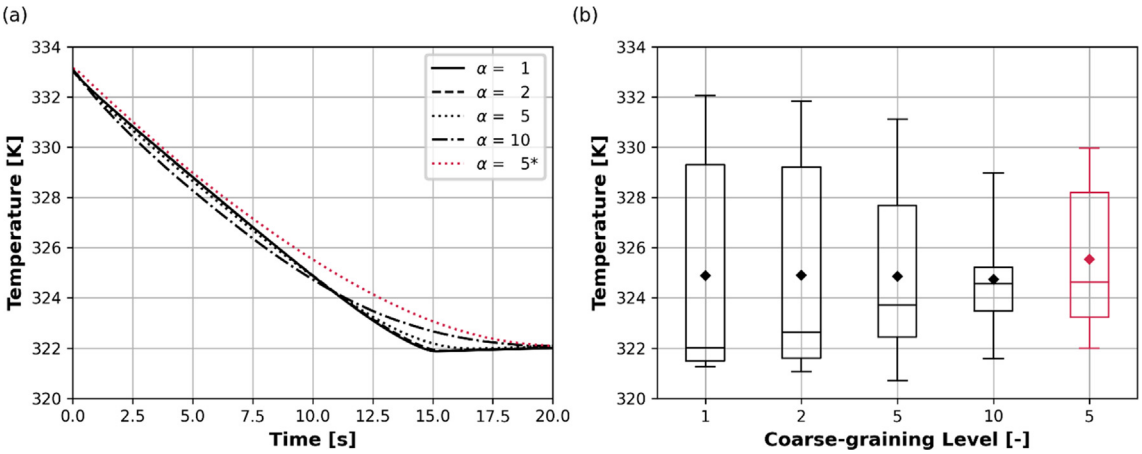

Fig. 3. (a) Mean particle temperature observed at various coarse-graining levels. The red dotted line shows the results of a simulation without the coarse-graining model for mass transfer. (b) Box plot of the particle temperature distribution after 10 s simulation time. The diamonds mark the mean value, the line inside the box represents the median value, the box borders indicate the 1st and 3rd quartiles and the whiskers indicate the 5th and 95th percentile. The red box on the right shows a simulation for $\alpha = 5$ without using the coarse-graining model for mass transfer ($f_r = 1$). (For interpretation of the references to color in this figure legend, the reader is referred to the web version of this article.)

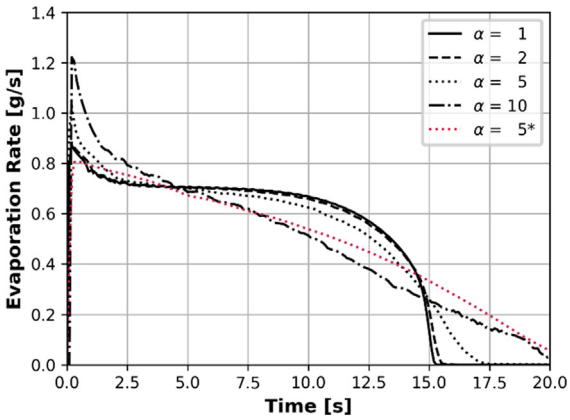

Fig. 4. Global evaporation rate observed at various coarse-graining levels. The red dotted line shows the results of a simulation without the coarse-graining model for mass transfer. (For interpretation of the references to color in this figure legend, the reader is referred to the web version of this article.)

$\alpha = 10$, we conclude that the necessary coarsening of the coupling grid is the main reason for the higher peaks observed at high coarse-graining levels.

After the initial peak, the evaporation rate in the case with extreme coarse graining (i.e., $\alpha = 10$) steadily decreases over time and the model fails to reproduce the constant and falling rate stage observed in the primary particle case. The different stages are observed for $\alpha = 5$, but disappear if the scaling rule for mass transfer (i.e., Eq. (14)) is disabled (see red dotted line in Fig. 4). The results show that the coarse-graining model for mass transfer improves the simulation performance. Also, the model delivers acceptable accuracy for coarse-graining levels up to 5, but cannot be used with confidence at higher levels.

3.2. Spray deposition model

Utilizing a similar setup as described above, the spray deposition model is also validated in a static bed. However, since only droplet-particle interaction is of interest, we do not simulate heat transport phenomena or airflow, i.e., it is a pure DEM simulation. To test the applicability of the model over a broad range of process conditions, particle volume fractions of 0.1, 0.3 and 0.6 are investigated. The spray nozzle is placed 400 mm above the particle bed, the droplet diameter is 20 μm and the opening angle of the spray cone is 23°. Fig. 5 shows the setup of the simulation and the distribution of spray droplets across the bed. The simulation parameters are stated in Table 1. To determine the amount of deposited coating versus the particle bed depth, the particle bed is divided vertically into 300 uniform layers. Every particle is assigned to the layer

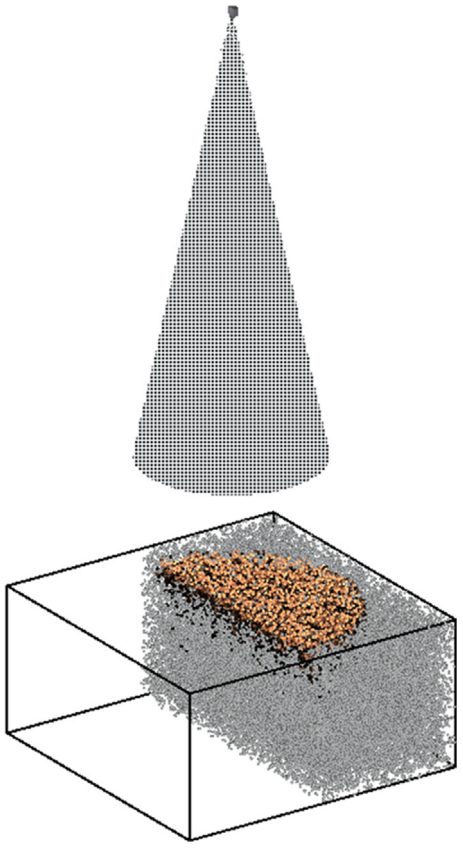

Fig. 5. Cross-section of the spray deposition simulation ($\alpha = 2$, $\phi_p = 0.1$). The dimensions of the box are 200 × 200 × 100 mm (LxWxH). Particles are colored according to the amount of deposited water.

that contains its center, and all droplets that are deposited on a particle contribute to the spray mass of this layer.

Fig. 6 shows a comparison of coarse-grained simulations with a simulation of primary particles as reference case at a particle volume fraction of 0.3. The red lines show the cumulative spray deposition over the bed depth (normalized with the primary particle diameter) for coarse-graining levels of 5 and 10 without utilizing a model for spray deposition (this is equivalent to an effective size factor of $f_r = 1$). As can be seen, the bed penetration scales approximately with the coarse-graining level α, causing a significant deviation from the reference case. In contrast, the simulations with the spray deposition model given by Eq. (27) perform very well: for $\alpha = 5$, hardly any difference to the reference case is observed up to a spray deposition of 80 %, followed by a minor overcorrection for the final 20 %. In summary 99 % of the spray is deposited at a normalized penetration depth of 5.1 for $\alpha = 5$ when using the model given by Eq. (27), compared to 7.8 for the reference case. The simulation results for $\alpha = 10$ shows a shift towards deeper bed penetration up to a normalized penetration depth of 5 primary particle diameters. However, the final penetration depth matches very well (8.4 vs 7.8 for 99 % spray deposition). Overall, Fig. 6 clearly highlights the necessity of a coarse-graining model for spray deposition, as the model significantly enhances the performance of the simulations.

In Fig. 7a we assess the model quality for coarse-graining ratios up to 10 in loose ($\phi_p = 0.1$) and dense ($\phi_p = 0.6$) packings. Generally, a good agreement between coarse-grained simulations and the reference cases is observed. Compared to the reference case, slightly smaller spray penetration depths are recorded for the loose packing simulations across all coarse-graining levels: 50 % of the spray are deposited at a normalized depth of 4.3 for the reference case, compared to a normalized depth of 4.0 and 3.3 for $\alpha = 2$ and $\alpha = 5$, respectively. For the dense bed, the simulation with $\alpha = 2$ delivers excellent results (50 % deposition at a depth of 0.51 versus 0.56 for the reference case), while the penetration depth increases for higher coarse-graining levels. There are two reasons for this deviation: (i) the theoretical accuracy limit and (ii) the physical limit of the proposed modelling approach. The theoretical accuracy arises from how the spray deposition is measured. Since the position of a particle is assigned to its center, but droplets can deposit anywhere on the surface, an error up to a normalized penetration depth of $\alpha/2$ is possible. Removing this theoretical "sub-particle resolution" accuracy could be part of future investigations, and

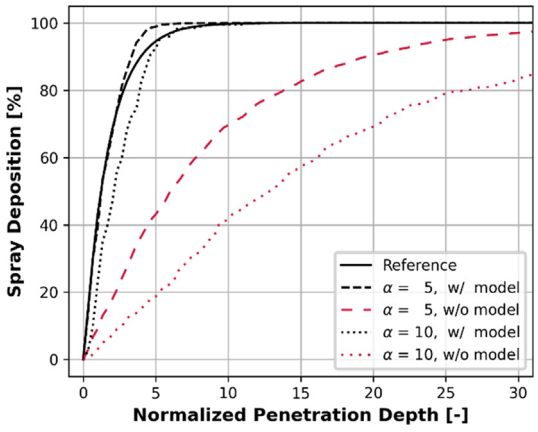

Fig. 6. Comparison of coarse-grained simulations with and without (i.e., $f_r = 1$) using the semi-empirical model given by Eq. (27). A simulation with primary particles is used as the reference case, the volume fraction of the particle bed is 0.3. The spray penetration depth was normalized with the diameter of a primary particle.

was not followed further. The physical limit is a constraint of the modelling approach: by increasing the effective diameter of the particles in the system, the particles grow and gaps between neighboring particles become narrower. At the point where the particles touch, no droplets can pass in between them anymore. Hence, if all gaps in the powder bed are closed, a further increase in effective diameter will not affect the distribution of droplets across the particles anymore.

The effect of the physical limit on the simulation result becomes more relevant in dense simulations at high coarse-graining levels. Fig. 7b shows the influence of the effective size factor on the model performance in a setup where the physical limit of the model comes into effect. The particle volume fraction in the investigated static bed is 0.6, with the coarse-graining level being set to 10. The data indicated as "reference" case shows the result of a simulation with primary particles. The parameters used for the simulations are given in Table 2. The limited capability of the model to reproduce the reference case is shown by a run with an effective size factor of 100. While in the reference case 99 % of the droplets are deposited at a normalized bed depth of 2.4, approximately 86 % are deposited at the same depth for $f_r = 100$. The same result is already obtained for an effective size factor of 12.6, confirming that the actual value of the effective size factor is not important anymore as soon as the physical limit is reached. The model proposed in this work (i.e., Eq. (27)) comes close to that limit, and significantly outperforms the correlation given by Eq. (24). Only minor improvements would be possible with a more complex model, since it would not be possible to overcome the theoretical accuracy limit (i.e., error in the normalized penetration depth of $\alpha/2$) mentioned before. Concluding the above, the presented coarse-graining approach is capable to model spray deposition for monodisperse systems with sufficient accuracy over the whole range of possible particle volume fractions.

3.3. Use case: top-spray fluidized bed coater

In this section, we validate the coarse-graining approach in a simulation of a Glatt GPCG-2 top-spray coater. Contrary to the previous two validation studies, which focused on the coarse-graining of a single mechanism, all models (including the collision dynamics, drag, heat and mass transfer, and spray deposition) are combined in the top-spray coating simulation. The reference case consists of 5 million particles, leading to a fill weight of 3.4 kg. The coating suspension consists of 90 % water and 10 % solids (density: 1300 kg/m^3). The spray rate is set to 20 g/min and the spray droplets have a diameter of 25 µm. The opening angle of the spray cone is 30°. With a fluidization velocity of 1 m/s, the coater is operated in the bubbling flow regime (the minimum fluidization velocity of the particles is 0.7 m/s). At the outlet on top of the device a pressure boundary condition of 1 bar is applied. The CFD mesh of the top-spray coater contains 240,000 cells, with a representative cell size (following the definition of [76]) of 5 mm. The setup and dimensions are pictured in Fig. 8, the material properties are given in Table 1 and the DEM contact parameters are given in Table 3. The contact parameters were not calibrated to a specific material since it would add little to the findings of our present study, but typical values have been used. The stiffness parameters of DEM-based simulations are chosen based on a tradeoff between maximum observed overlap and computational speed (real-world particle stiffnesses would require extreme computation times that would not lead to an increase in the predictive capability of the simulation). The damping parameters were chosen to realize a coefficient of restitution of 0.7, which is typical for granule particles.

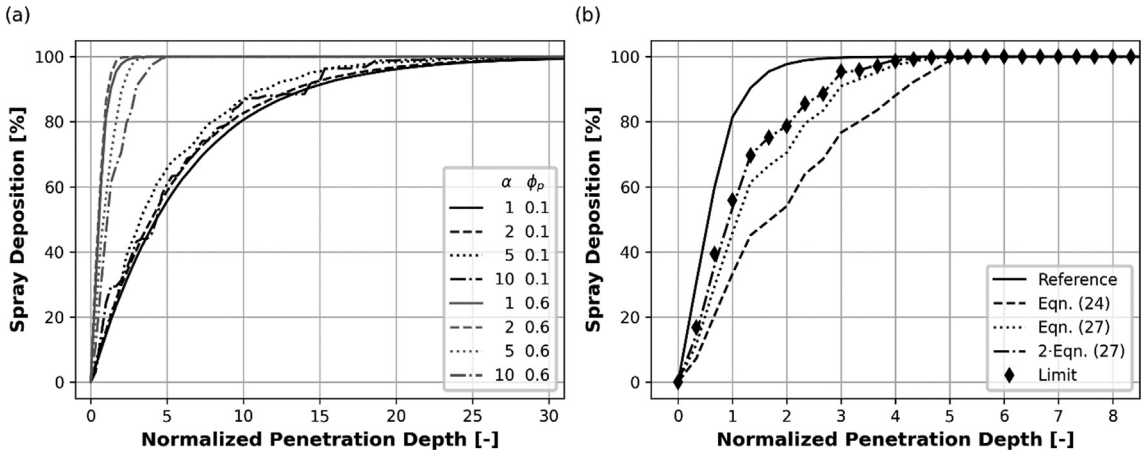

Fig. 7. (a) Validation of the spray deposition model for particle volume fractions of 0.1 and 0.6. (b) Comparison of simulation results for various effective size factors (see Table 2) at a coarse-graining level of $\alpha = 10$ and a particle volume fraction of $\varphi_p = 0.6$. The Eq. (27) curve in panel (b) is identical to the $\alpha = 10$ and $\varphi_p = 0.6$ case in panel (a).

Table 2
Parameters and results to evaluate the physical limit of the coarse-graining model for spray deposition.

Case	Coarse-graining level	Effective size factor	Spray deposition at a normalized bed depth of 2.4
Reference	1	1.0	99 %
Eq. (24)	10	3.2	65 %
Eq. (27)	10	6.3	80 %
2·Eq. (27)	10	12.6	86 %
Limit	10	100.0	86 %

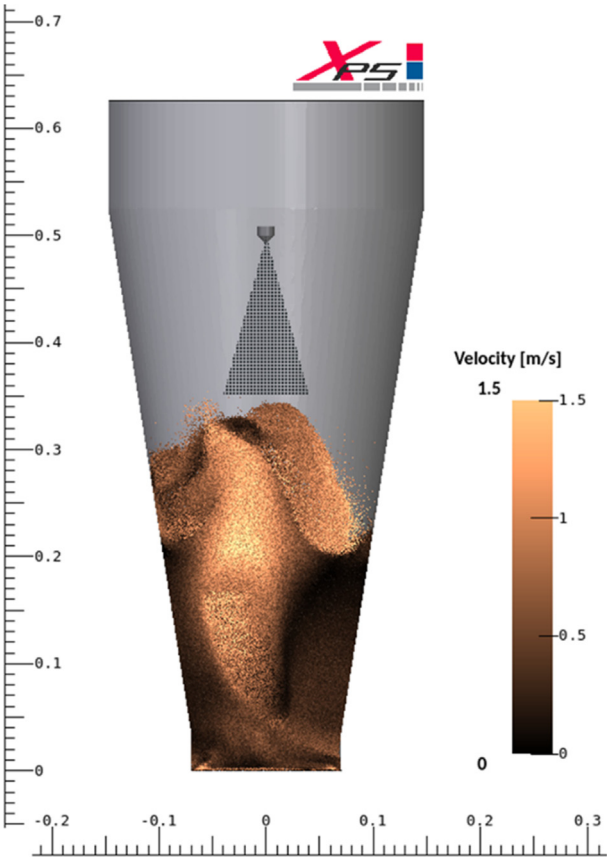

Fig. 8. Snapshot of the top-spray coating simulation (reference case). Ruler dimensions are in m.

Table 3
Contact parameters for the linear spring-dashpot model.

Property	Unit	Value
Normal spring stiffness	N/m	3000
Tangential spring stiffness	N/m	2400
Sliding friction coefficient	–	0.05
Rolling friction coefficient	–	0.125
Coefficient of restitution	–	0.7

Given that the initial particle temperature was set to the inlet air temperature, the temperature gradually decreases over time (because of the latent heat of evaporation) until it converges towards a statistical steady-state value. Assuming that in steady-state conditions the global evaporation rate equals the spray rate, the exhaust air temperature can be estimated by considering the enthalpy of the fluidization air and the cooling rate of the spray liquid according to Eq. (28). Let us suppose that the mean particle temperature would be the average of inlet and exhaust air temperature, then we would obtain a value of 312 K for the equilibrium state. The characteristic time scale is 50 s according to Eq. (29). However, the actual simulation time necessary to arrive at steady-state conditions would be much longer due to the exponential decrease of the temperature over time. Such long simulation times are computationally not feasible and therefore we simulate only 20 s of process time.

$$T_{ex} = T_{in} - \frac{w_l \dot{m}_{spray} \Delta H_v}{\dot{m}_{air} c_{p,air}} \tag{28}$$

$$\tau_s = \frac{\sum m_p c_p \Delta T}{w_l \dot{m}_{spray} \Delta H_v} \tag{29}$$

In Eq. (28), T_{ex} and T_{in} are the temperature of the exhaust and inlet air, w_l is the liquid mass fraction of the coating solution, $\dot{m}_{spray}$ is the spray rate, ΔH_v is the latent heat of evaporation and $\dot{m}_{air}$ and $c_{p,air}$ are the mass flow and the heat capacity of the fluidization air. In Eq. (29), τ_s is the characteristic time to reach the steady state, $\sum m_p$ is the (total) batch mass of the particles, c_p is the specific heat capacity of the particles, and ΔT is the difference between the initial and equilibrium particle temperature.

Fig. 9a shows the evolution of the mean particle temperature over time for various coarse-graining levels. Coarse-graining levels 2 and 5 agree excellently with the reference case, as the temperature difference after 20 s is only 0.01 K and 0.03 K, respectively. For $\alpha = 10$, the difference at the end is 0.23 K. Similarly, the particle

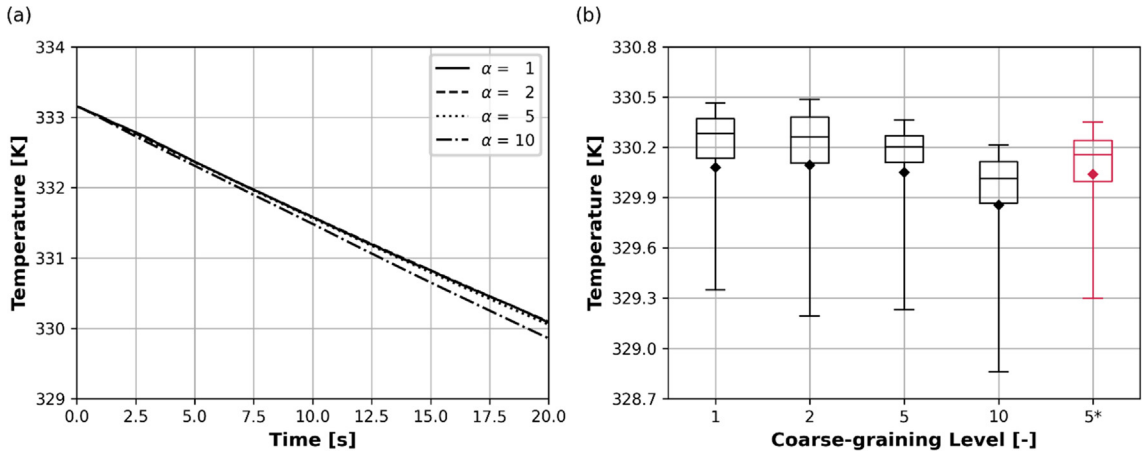

Fig. 9. (a) Temporal evolution of the mean particle temperature and (b) boxplot of the particle temperature distribution after 20 s of simulated time in a top-spray fluidized bed coater. The diamonds mark the mean value, the line inside the box represents the median value, the box borders indicate the 1st and 3rd quartiles and the whiskers indicate the 5th and 95th percentile. The red box on the right shows a simulation for $\alpha = 5$ without using the coarse-graining model for spray deposition ($f_r = 1$). (For interpretation of the references to color in this figure legend, the reader is referred to the web version of this article.)

temperature distribution at the end of the simulation agrees very well for $\alpha = 2$ and $\alpha = 5$, while lower temperatures are observed for $\alpha = 10$ (Fig. 9b). Two reasons were identified for the deviations for $\alpha = 10$: (i) the coarse coupling grid and (ii) insufficient fluidization. To detect the effect of the coupling grid, we conducted a simulation with primary particles, but use the coupling grid for $\alpha = 10$. The temperature difference at the end of the simulation is 0.08 K, accounting for 35 % of the error occurring for $\alpha = 10$. The fluidization behavior can be characterized by the time-averaged vertical particle velocity (Fig. 10a). The boxplots show that the fluidization is hindered for $\alpha = 10$. Most likely, there is a significant effect of the dryer geometry on the particle motion. The bottom of the coater has a diameter of 140 mm, compared to a parcel diameter of 10 mm. Sphere packing simulations in a cylinder reveal that wall effects (i.e., local ordering of particles) occur up to a distance of five particle diameters from the wall [77]. Hence, only a comparably small fraction of parcels is not affected by the geometry. Another reason for the poor fluidization could have been the coarse coupling grid. However, we observed similar fluidization behavior in primary particle simulations with (i) fine and (ii) coarse coupling grids, indicating that the poor fluidization for $\alpha = 10$ is solely caused by the large parcel diameter.

Comparing simulations for $\alpha = 5$ with and without using the spray deposition model shows that the particle temperature distribution does not vary significantly (Fig. 9b). Hence, if one wants to evaluate only the temperature in a spray coater, using the coarse-graining model for spray deposition appears not absolutely necessary. However, we will show in the next paragraphs that this is not true for other properties, such as the wet surface ratio, evaporation rate and coating mass distribution.

Fig. 10b shows the probability density function (PDF) of the wet-to-total particle surface area ratio of at least partially wetted particles at the end of the simulation. No significant deviations to the reference case are observed up to a coarse-graining level of $\alpha = 5$. For $\alpha = 10$, the trend looks very similar, but distinct fluctuations are present. If the scaling law for spray deposition is disabled, the droplets are distributed over more particles, leading to lower values of the wet surface ratio. In that case, no particle has a wet surface ratio greater than 10 %, a value that is exceed by 3.2 % of the wet particles in the reference case.

Fig. 11a shows the temporal evolution of the one-second moving average of the global evaporation rate, i.e., the sum of the evaporation rates of all particles. For all cases, the evaporation rate fluctuates around the same value of 0.3 g/s, which equals the liquid

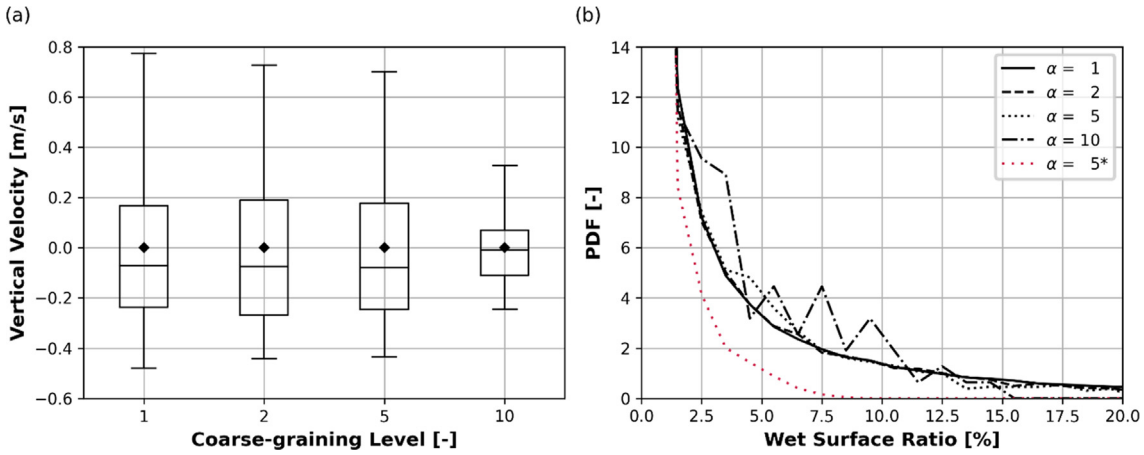

Fig. 10. (a) Boxplot of the vertical particle velocity distribution, time-averaged over the last five seconds. The diamonds mark the mean value, the line inside the box represents the median value, the box borders indicate the 1st and 3rd quartiles and the whiskers indicate the 5th and 95th percentile. (b) Probability density function of the wet surface ratio at a simulation time of 20 s. The red curve shows a simulation for $\alpha = 5$ without using the coarse-graining model for spray deposition ($f_r = 1$). (For interpretation of the references to color in this figure legend, the reader is referred to the web version of this article.)

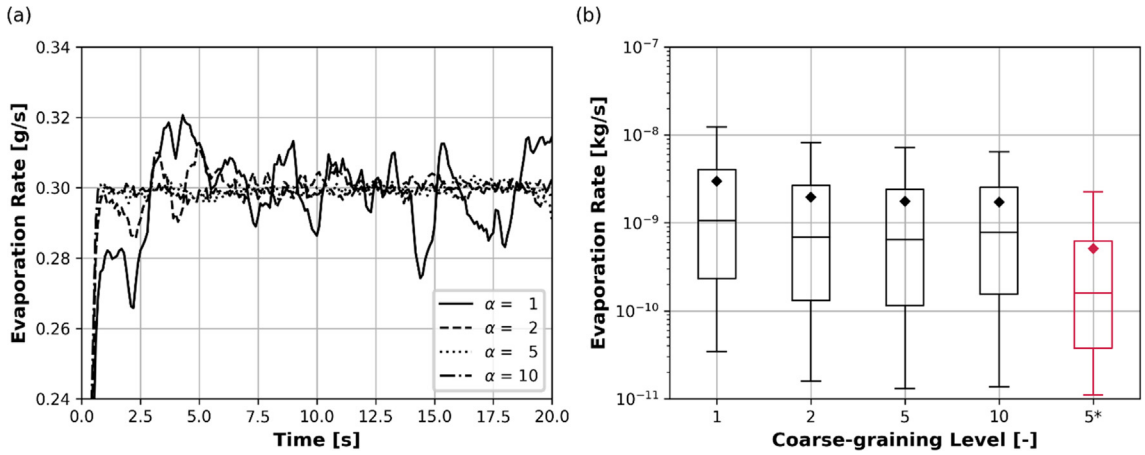

Fig. 11. (a) Temporal evolution of the global evaporation rate (to enhance visibility, the graph shows the one-second moving average). (b) Boxplot of the per-particle evaporation rate distribution, time-averaged over the last five seconds. Only wet particles are considered in (b). The diamonds mark the mean value, the line inside the box represents the median value, the box borders indicate the 1st and 3rd quartiles and the whiskers indicate the 5th and 95th percentile. The red box on the right shows a simulation for $\alpha = 5$ without using the coarse-graining model for spray deposition ($f_r = 1$). (For interpretation of the references to color in this figure legend, the reader is referred to the web version of this article.)

spray rate. This condition is necessary for steady-state, so that the liquid mass in the system does not accumulate. While the mean value is constant for all runs, the amplitude of the fluctuations decreases with increasing coarse-graining level: the coefficients of variation are 11.5 %, 8.8 %, 8.8 % and 8.2 % for coarse-graining levels of 1, 2, 5 and 10, respectively.

Fig. 11b illustrates the distribution of the time-averaged per-particle evaporation rate. Given the fact that the values span over almost three orders of magnitude, the coarse-grained simulations match the reference case very well. Comparing the results with a simulation where the model is disabled highlights the importance of the spray deposition model: the time-averaged per-particle evaporation rate in the reference case is $3 \cdot 10^{-9}$ kg/s, compared to $2 \cdot 10^{-9}$ kg/s with, and $5 \cdot 10^{-10}$ kg/s without the model at $\alpha = 5$.

Thus, with increasing coarse graining level the per-particle evaporation rate drops (without the spray model this drop is −83 %, while −33 % with the spray model). This reflects the fact that more particles are contacted with droplets, i.e., the deposition of droplets on the particles is more uniform in coarse-grained simulations compared to the reference case. This reduced per-particle evaporation rate is caused by the fundamental assumption that all particles inside a coarse-grained parcel have the same properties. This reduces the occurrence of extreme conditions and leads to the observed more uniform droplet distribution across the particle bed. While in the reference case roughly 76 % of the particles collected at least a single droplet during 20 s simulation time, this value increases to nearly 91 % for the simulation with $\alpha = 5$ (Fig. 12a). The decline to 83 % for $\alpha = 10$ is a result of poor mixing because of the insufficient fluidization as already mentioned before. Due to the cubic scaling of the number of particles, 125 primary particles have to be coated for a single parcel with coarse-graining factor 5. However, those particles would shield each other, so that only a fraction actually would receive coating during a single pass through the spray zone. This can also be observed in the final solid coating distribution (Fig. 12b): while the mean coating mass is very close to the reference case, the maxima and minima are smaller for the coarse-grained simulations. The minimal deposited solid mass per particle is given by $\frac{x_s m_d}{\alpha^3}$, where x_s is the solid mass fraction in the coating suspension, and m_d is the mass of a single droplet. Similarly, the maximal coating mass is distributed

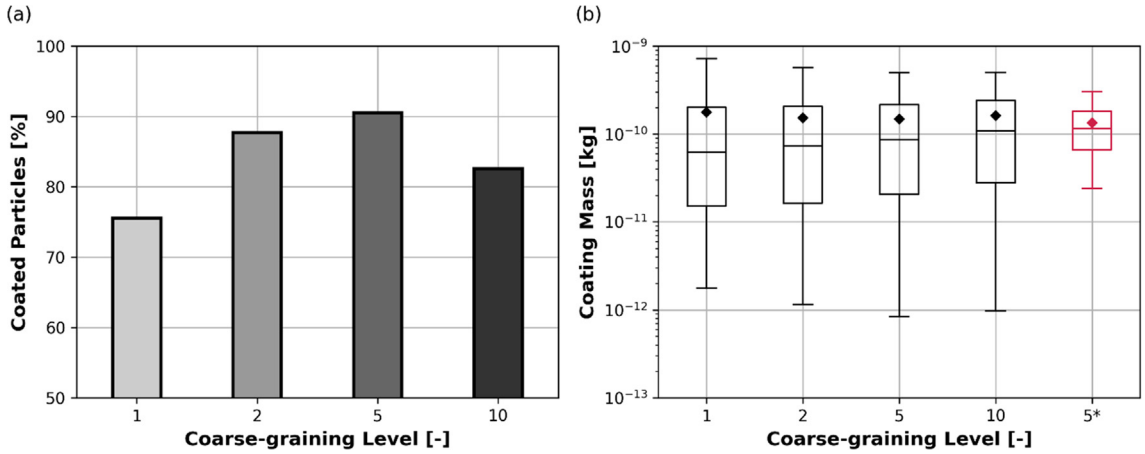

Fig. 12. (a) Percentage of particles, on which at least a single droplet was deposited after 20 s of simulated time. (b) Boxplot of the coating mass distribution after 20 s simulation time, considering only coated particles. The diamonds mark the mean value, the line inside the box represents the median value, the box borders indicate the 1st and 3rd quartiles and the whiskers indicate the 5th and 95th percentile. The red box on the right shows a simulation for $\alpha = 5$ without using the coarse-graining model for spray deposition ($f_r = 1$). (For interpretation of the references to color in this figure legend, the reader is referred to the web version of this article.)

across α^3 particles, causing the lower extreme values in the distribution. Although the maximum and minimum values differ from the reference case, the model performs very well when considering the mean and median values. The importance of the spray deposition model becomes evident, when the results are compared to a coarse-grained simulation without the spray model, in which the distribution is almost two orders of magnitude narrower than the reference case.

We finally would like to comment on the computational resources needed for our simulations: they were all carried out on a single workstation equipped with an AMD Ryzen 7 2700X CPU (5 cores were used for CFD) and an NVIDIA GeForce GTX 1080Ti GPU (XPS is a GPU-based DEM software). The wall clock time for simulating 20 s process time was 322 h (13.4 days) for the primary particle case, compared to 68 h (2.8 days) for a case with a coarse-graining level of 5. Thus, a speed-up factor of 4.7 was realized. While for the primary particle simulation (involving 5 million particles) DEM was the time limiting part of the computation, DEM computations were faster than the CFD simulation in the coarse-grained simulation with $\alpha = 5$ (involving 40,000 parcels). Hence, for systems containing a larger number of particles, or in case smaller DEM time steps are used, the speed-up factor might be even higher. If DEM is the limiting part of the computation, a further speed-up could be obtained by switching from an energy-based scaling to a dimensionless-overlap-based scaling for the contact parameters. The reason for this would be the larger time step that can be used in the coarse-grained simulation. For example, Tausendschön et al. [53] reported a reduction of computational time by a factor of 30 for $\alpha = 4$ when using such a scaling.

4. Conclusion

The parcel-based method is commonly used to reduce the computational effort of (CFD-)DEM simulations, but some models are still missing if one wants to simulate spray coating processes [30,53]. Therefore, we extend existing coarse-graining approaches by models for mass transfer and spray deposition. The models were separately validated in static bed simulations. Simulations of a top-spray fluidized bed coater reveal that the models are capable of correctly reproducing the temperature, evaporation rate and coating mass distributions when compared to simulations with original-sized particles. However, there is some loss of information regarding extreme conditions in coarse-grained simulations due to the (imposed) equality of all particles inside a parcel. This also leads to a higher percentage of coated particles in coarse-grained simulations. Hence, a coating distribution model on sub-parcel level could be a fruitful path to follow to further improve the precision of coarse-grained simulations.

Our results indicate that the presented approach can be reliably used up to a coarse-graining factor of 5 (the same value was proposed by Tausendschön et al. [53] for cohesive gas-particle systems). This will be true as long as there are no geometrical restrictions that could influence the particle motion. For larger coarse-graining ratios fluidization could not be reproduced satisfactory due to the violation of geometric similarity between parcels and walls. This problem could possibly be tackled by correcting the overlap distance between parcels and walls, analogous to the approach adopted by Kanjilal and Schneiderbauer [56] for polydisperse systems. Continuative investigations that focus on developing corrections for drag and mass transfer rates, similar to what was proposed by Radl and Sundaresan [74], would be valuable to counter information loss regarding flow and particle dynamics in case of high coarse-graining levels.

With the proposed models, it is possible to reduce the computational effort of detailed coating simulations by a factor of 4.7 (at $\alpha = 5$), while still capturing all relevant physics of such a process. Additionally, the models can be used to simulate related processes and phenomena such as droplet drying (i.e., adopting our mass transfer model) or radiation (i.e., adopting our spray deposition model). An extension of our newly introduced models to polydisperse systems and non-spherical particles have to be evaluated in future work. Since our ray tracing algorithm accounts for the geometrical arrangement (and of course the size) of particles, we do expect that our models are applicable without requiring major modifications. However, one must consider that higher particle volume fractions are possible, and therefore the physical limit discussed in section 3.2 could become more relevant in dense packings.

Declaration of Competing Interest

The authors declare that they have no known competing financial interests or personal relationships that could have appeared to influence the work reported in this paper.

Acknowledgement

RCPE is a K1 COMET Centre within the COMET – Competence Centres for Excellent Technologies programme. The COMET programme is operated by the Austrian Research Promotion Agency (FFG) on behalf of the Federal Ministry for Transport, Innovation and Technology (BMVIT) and the Federal Ministry for Digital and Economic Affairs (BMDW). Our projects are also funded by Land Steiermark and the Styrian Business Development Agency (SFG).

Appendix A

Derivation of Eq. (25)

The volume fraction ϕ_p for a monodisperse particle system calculated as.

$$\phi_p = \frac{N_p V_p}{V_{tot}} \tag{A1}$$

where N_p is the number of particles, V_p is the volume of a single particle and V_{tot} is the total volume of the domain.

Starting with point particles, we add a finite volume element ΔV to each particle. Considering Eq. (A 1) the contribution to the volume fraction in case that none of these additional volumes overlaps can be calculated as follows:

$$\delta_\phi = \frac{\Delta V N_p}{V_{tot}} = \frac{\Delta V \phi_p}{V_p} \tag{A2}$$

However, when adding a finite volume element to a particle, it will partially overlap with other particles. In case the volume element is randomly placed in space, the fraction of the volume element that overlaps is statistically equal to the current volume fraction. For example, if the volume fraction is 0.3, then we assume that 30 % of the new element are overlapping, while 70 % fill empty space and consequently increase the particle volume fraction. After adding n volume elements to each particle, the particle volume fraction in the system can be calculated as [78]:

$$\phi_p = 1 - e^{-\delta_\phi n}$$

$$\Rightarrow n = -\frac{ln(1-\phi_p)}{\delta_\phi} \tag{A3}$$

Therefore, to obtain a certain volume fraction, n volume elements are necessary. The number of volume elements Δn needed to increase the volume fraction from an initial value $\phi_{p,0}$ (e.g., the

original system without coarse-graining) to a higher value $\phi_{p,1}$ (e.g., the coarse-grained case) is given by the difference between the number of elements necessary to obtain $\phi_{p,1}$ and $\phi_{p,0}$:

$$\Delta n = n_1 - n_0 = -\frac{ln\left(\frac{1-\phi_{p,1}}{1-\phi_{p,0}}\right)}{\delta_\phi} \tag{A4}$$

Introducing the effective size factor f_r, the volume of all coarse-grained particles in the volume V_{tot} is connected to the volume of the original particles via.

$$V_{p,1} = f_r^3 V_{p,0} = V_{p,0} + \Delta n \Delta V \tag{A5}$$

$$f_r^3 = 1 + \frac{\Delta n \Delta V}{V_p} = 1 + \frac{\Delta n \delta_\phi}{\phi_{p,0}} \tag{A6}$$

Substituting Eqs. (21) and (A 4) into Eq. (A 6) leads to.

$$f_r^3 = 1 - \frac{ln\left(\frac{1-f_r \alpha \phi_{p,0}}{1-\phi_{p,0}}\right)}{\phi_{p,0}} \tag{A7}$$

which is equivalent to Eq. (25).

References

[1] N. Govender, R.K. Rajamani, S. Kok, D.N. Wilke, Discrete element simulation of mill charge in 3D using the BLAZE-DEM GPU framework, Miner. Eng. 79 (2015) 152–168, https://doi.org/10.1016/j.mineng.2015.05.010.

[2] E. Davide, S. Doug, E. Erik, V. Alex, Applications of finite/discrete element modeling to rock engineering problems, Int. J. Geomech. 13 (5) (Oct. 2013) 565–580, https://doi.org/10.1061/(ASCE)GM.1943-5622.0000238.

[3] O. Catherine, Particle-based discrete element modeling: geomechanics perspective, Int. J. Geomech. 11 (6) (2011) 449–464, https://doi.org/10.1061/(ASCE)GM.1943-5622.0000024.

[4] J.M. Boac, R.P.K. Ambrose, M.E. Casada, R.G. Maghirang, D.E. Maier, Applications of discrete element method in modeling of grain postharvest operations, Food Eng. Rev. 6 (4) (2014) 128–149.

[5] Z. Chen, C. Wassgren, E. Veikle, K. Ambrose, Determination of material and interaction properties of maize and wheat kernels for DEM simulation, Biosyst. Eng. 195 (2020) 208–226, https://doi.org/10.1016/j.biosystemseng.2020.05.007.

[6] H. Kureck, N. Govender, E. Siegmann, P. Boehling, C. Radeke, J.G. Khinast, Industrial scale simulations of tablet coating using GPU based DEM: A validation study, Chem. Eng. Sci. 202 (2019) 462–480, https://doi.org/10.1016/j.ces.2019.03.029.

[7] S. Bin Yeom, E. Ha, M. Kim, S.H. Jeong, S.J. Hwang, D.H. Choi, Application of the discrete element method for manufacturing process simulation in the pharmaceutical industry, Pharmaceutics 11 (8) (2019), https://doi.org/10.3390/pharmaceutics11080414.

[8] E. Siegmann, T. Forgber, P. Toson, M.C. Martinetz, H. Kureck, T. Brinz, S. Manz, T. Grass, J. Khinast, Powder flow and mixing in different tablet press feed frames, Adv. Powder Technol. 31 (2) (2020) 770–781, https://doi.org/10.1016/j.apt.2019.11.031.

[9] P. Toson, E. Siegmann, M. Trogrlic, H. Kureck, J. Khinast, D. Jajcevic, P. Doshi, D. Blackwood, A. Bonnassieux, P.D. Daugherity, M.T. am Ende, Detailed modeling and process design of an advanced continuous powder mixer, Int. J. Pharm. 552 (1-2) (2018) 288–300.

[10] P. Loidolt, S. Madlmeir, J.G. Khinast, Mechanistic modeling of a capsule filling process, Int. J. Pharm. 532 (1) (2017) 47–54, https://doi.org/10.1016/j.ijpharm.2017.08.125.

[11] S. Madlmeir, P. Loidolt, J.G. Khinast, Study of the capsule-filling dosator process via calibrated DEM simulations, Int. J. Pharm. 567 (2019) 118441, https://doi.org/10.1016/j.ijpharm.2019.06.032.

[12] S. Kuang, M. Zhou, A. Yu, CFD-DEM modelling and simulation of pneumatic conveying: A review, Powder Technol. 365 (2020) 186–207, https://doi.org/10.1016/j.powtec.2019.02.011.

[13] E. Dianyu, Validation of CFD–DEM model for iron ore reduction at particle level and parametric study, Particuology 51 (2020) 163–172, https://doi.org/10.1016/j.partic.2019.10.008.

[14] P. Boehling, D. Jacevic, F. Detobel, J. Holman, L. Wareham, M. Metzger, J.G. Khinast, Validating a Numerical Simulation of the ConsiGma(R) Coater, AAPS PharmSciTech 22 (1) (2021), https://doi.org/10.1208/s12249-020-01841-7.

[15] P. Boehling, G. Toschkoff, K. Knop, P. Kleinebudde, S. Just, A. Funke, H. Rehbaum, J.G. Khinast, Analysis of large-scale tablet coating: modeling, simulation and experiments, Eur. J. Pharm. Sci. 90 (2016) 14–24.

[16] X. Liu, W. Zhong, Minimum spouting velocity of binary mixture with non-spherical particles, Adv. Powder Technol. 33 (3) (2022) 103448, https://doi.org/10.1016/j.apt.2022.103448.

[17] Z. Jiang, A. Bück, E. Tsotsas, CFD–DEM study of residence time, droplet deposition, and collision velocity for a binary particle mixture in a Wurster fluidized bed coater, Dry. Technol. 36 (6) (2018) 638–650, https://doi.org/10.1080/07373937.2017.1319852.

[18] D. Jajcevic, E. Siegmann, C. Radeke, J.G. Khinast, Large-scale CFD–DEM simulations of fluidized granular systems, Chem. Eng. Sci. 98 (2013) 298–310, https://doi.org/10.1016/J.CES.2013.05.014.

[19] S. Pietsch, S. Heinrich, K. Karpinski, M. Müller, M. Schönherr, F. Kleine Jäger, CFD-DEM modeling of a three-dimensional prismatic spouted bed, Powder Technol. 316 (2017) 245–255, https://doi.org/10.1016/j.powtec.2016.12.046.

[20] Y. Zhang, Y. Zhao, L. Lu, W. Ge, J. Wang, C. Duan, Assessment of polydisperse drag models for the size segregation in a bubbling fluidized bed using discrete particle method, Chem. Eng. Sci., vol. 160, no. November 2016, pp. 106–112, 2017, doi: https://doi.org/10.1016/j.ces.2016.11.028.

[21] V. Agrawal, Y. Shinde, M.T. Shah, R.P. Utikar, V.K. Pareek, J.B. Joshi, Effect of drag models on CFD–DEM predictions of bubbling fluidized beds with Geldart D particles, Adv. Powder Technol. 29 (11) (2018) 2658–2669, https://doi.org/10.1016/j.apt.2018.07.014.

[22] P. Böhling, J.G. Khinast, D. Jajcevic, C. Davies, A. Carmody, P. Doshi, M.T. Am Ende, A. Sarkar, Computational fluid dynamics-discrete element method modeling of an industrial-scale wurster coater, J. Pharm. Sci. 108 (1) (2019) 538–550.

[23] A. Sarkar et al., Multiscale modeling of a pharmaceutical fluid bed coating process using CFD/DEM and population balance models to predict coating uniformity, in: Chemical Engineering in the Pharmaceutical Industry, 2nd ed., 2019, pp. 419–450.

[24] L. Fries, S. Antonyuk, S. Heinrich, S. Palzer, DEM-CFD modeling of a fluidized bed spray granulator, Chem. Eng. Sci. 66 (11) (2011) 2340–2355, https://doi.org/10.1016/j.ces.2011.02.038.

[25] M. Heine, S. Antonyuk, L. Fries, G. Niederreiter, S. Heinrich, S. Palzer, Modeling of the spray zone for particle wetting in a fluidized bed, Chemie-Ingenieur-Technik 85 (3) (2013) 280–289, https://doi.org/10.1002/cite.201200148.

[26] G. Toschkoff, S. Just, A. Funke, D. Djuric, K. Knop, P. Kleinebudde, G. Scharrer, J. G. Khinast, Spray models for discrete element simulations of particle coating processes, Chem. Eng. Sci. 101 (2013) 603–614, https://doi.org/10.1016/j.ces.2013.06.051.

[27] P. Boehling, G. Toschkoff, S. Just, K. Knop, P. Kleinebudde, A. Funke, H. Rehbaum, P. Rajniak, J.G. Khinast, Simulation of a tablet coating process at different scales using DEM, Eur. J. Pharm. Sci. 93 (2016) 74–83.

[28] V.S. Sutkar, N.G. Deen, A.V. Patil, V. Salikov, S. Antonyuk, S. Heinrich, J.A.M. Kuipers, CFD-DEM model for coupled heat and mass transfer in a spout fluidized bed with liquid injection, Chem. Eng. J. 288 (2016) 185–197, https://doi.org/10.1016/j.cej.2015.11.044.

[29] D. Suzzi, S. Radl, J.G. Khinast, Local analysis of the tablet coating process: Impact of operation conditions on film quality, Chem. Eng. Sci. 65 (21) (2010) 5699–5715, https://doi.org/10.1016/j.ces.2010.07.007.

[30] M. Askarishahi, M.-S. Salehi, S. Radl, Full-physics simulations of spray-particle interaction in a bubbling fluidized bed, AIChE J. 63 (7) (2017) 2569–2587, https://doi.org/10.1002/aic.15616.

[31] T. Tsory, N. Ben-Jacob, T. Brosh, A. Levy, Thermal DEM-CFD modeling and simulation of heat transfer through packed bed, Powder Technol. 244 (2013) 52–60, https://doi.org/10.1016/j.powtec.2013.04.013.

[32] S. Wang, K. Luo, C. Hu, J. Lin, J. Fan, CFD-DEM simulation of heat transfer in fluidized beds: Model verification, validation, and application, Chem. Eng. Sci. 197 (2019) 280–295, https://doi.org/10.1016/j.ces.2018.12.031.

[33] Z. Li, M. van Sint Annaland, J.A.M. Kuipers, N.G. Deen, Effect of superficial gas velocity on the particle temperature distribution in a fluidized bed with heat production, Chem. Eng. Sci. 140 (2016) 279–290, https://doi.org/10.1016/j.ces.2015.10.020.

[34] T. Forgber, S. Radl, A novel approach to calculate radiative thermal exchange in coupled particle simulations, Powder Technol. 323 (2018) 24–44, https://doi.org/10.1016/j.powtec.2017.09.014.

[35] E.F. Johnson, İ. Tarı, D. Baker, Radiative heat transfer in the discrete element method using distance based approximations, Powder Technol. 380 (2021) 164–182, https://doi.org/10.1016/j.powtec.2020.11.050.

[36] Z. Jiang, C. Rieck, A. Bück, E. Tsotsas, Modeling of inter- and intra-particle coating uniformity in a Wurster fluidized bed by a coupled CFD-DEM-Monte Carlo approach, Chem. Eng. Sci. 211 (2020) 115289, https://doi.org/10.1016/j.ces.2019.115289.

[37] S. Madlmeir, T. Forgber, M. Trogrlic, D. Jajcevic, A. Kape, L. Contreras, A. Carmody, P. Liu, C. Davies, A. Sarkar, J.G. Khinast, Quantifying the coating yield by modeling heat and mass transfer in a Wurster fluidized bed coater, Chem. Eng. Sci. 252 (2022) 117505, https://doi.org/10.1016/j.ces.2022.117505.

[38] M.S. van Buijtenen, W.J. van Dijk, N.G. Deen, J.A.M. Kuipers, T. Leadbeater, D.J. Parker, Numerical and experimental study on multiple-spout fluidized beds, Chem. Eng. Sci. 66 (11) (2011) 2368–2376, https://doi.org/10.1016/j.ces.2011.02.055.

[39] L. Li, J. Remmelgas, B.G.M. van Wachem, C. von Corswant, M. Johansson, S. Folestad, A. Rasmuson, Residence time distributions of different size particles in the spray zone of a Wurster fluid bed studied using DEM-CFD, Powder Technol. 280 (2015) 124–134, https://doi.org/10.1016/j.powtec.2015.04.031.

[40] M. Börner, A. Bück, E. Tsotsas, DEM-CFD investigation of particle residence time distribution in top-spray fluidised bed granulation, Chem. Eng. Sci. 161 (2017) 187–197, https://doi.org/10.1016/j.ces.2016.12.020.

[41] Z. Jiang, T. Hagemeier, A. Bück, E. Tsotsas, Color-PTV measurement and CFD-DEM simulation of the dynamics of poly-disperse particle systems in a pseudo-2D fluidized bed, Chem. Eng. Sci. 179 (2018) 115–132, https://doi.org/10.1016/j.ces.2018.01.013.

[42] A.V. Patil, E.A.J.F. Peters, J.A.M. Kuipers, Comparison of CFD-DEM heat transfer simulations with infrared/visual measurements, Chem. Eng. J. 277 (2015) 388–401, https://doi.org/10.1016/j.cej.2015.04.131.
[43] M. Trogrlić, S. Madlmeir, T. Forgber, S. Salar-Behzadi, A. Sarkar, P. Liu, L. Contreras, A. Carmody, A. Kape, J. Khinast, D. Jajčević, Numerical and experimental validation of a detailed non-isothermal CFD-DEM model of a pilot-scale Wurster coater, Powder Technol. 391 (2021) 97–113, https://doi.org/10.1016/j.powtec.2021.05.100.
[44] M. Marigo, E.H. Stitt, Discrete element method (DEM) for industrial applications: Comments on calibration and validation for the modelling of cylindrical pellets, KONA Powder Part. J. 32 (32) (2015) 236–252, https://doi.org/10.14356/kona.2015016.
[45] C.J. Coetzee, Review: Calibration of the discrete element method, Powder Technol. 310 (2017) 104–142, https://doi.org/10.1016/j.powtec.2017.01.015.
[46] T. Lichtenegger, S. Pirker, Recurrence CFD – A novel approach to simulate multiphase flows with strongly separated time scales, Chem. Eng. Sci. 153 (2016) 394–410, https://doi.org/10.1016/j.ces.2016.07.036.
[47] S. Madlmeir, T. Forgber, M. Trogrlic, D. Jajcevic, A. Kape, L. Contreras, A. Carmody, P. Liu, C. Davies, A. Sarkar, J.G. Khinast, Modeling the coating layer thickness in a pharmaceutical coating process, Eur. J. Pharm. Sci. 161 (2021) 105770, https://doi.org/10.1016/j.ejps.2021.105770.
[48] A. Di Renzo, E.S. Napolitano, F.P. Di Maio, Coarse-grain DEM modelling in fluidized bed simulation: a review, Processes 9 (2) (2021) 279, https://doi.org/10.3390/pr9020279.
[49] M. Sakai, S. Koshizuka, Large-scale discrete element modeling in pneumatic conveying, Chem. Eng. Sci. 64 (3) (2009) 533–539, https://doi.org/10.1016/j.ces.2008.10.003.
[50] C. Bierwisch, T. Kraft, H. Riedel, M. Moseler, Three-dimensional discrete element models for the granular statics and dynamics of powders in cavity filling, J. Mech. Phys. Solids 57 (1) (2009) 10–31, https://doi.org/10.1016/j.jmps.2008.10.006.
[51] Z. Jiang, K. Rai, T. Tsuji, K. Washino, T. Tanaka, J. Oshitani, Upscaled DEM-CFD model for vibrated fluidized bed based on particle-scale similarities, Adv. Powder Technol. 31 (12) (2020) 4598–4618, https://doi.org/10.1016/j.apt.2020.10.009.
[52] K. Washino, C.-H. Hsu, T. Kawaguchi, Y. Tsuji, Similarity Model for DEM Simulation of Fluidized Bed, J. Soc. Powder Technol. Japan 44 (3) (2007) 198–205, https://doi.org/10.4164/sptj.44.198.
[53] J. Tausendschön, J. Kolehmainen, S. Sundaresan, S. Radl, Coarse graining Euler-Lagrange simulations of cohesive particle fluidization, Powder Technol. 364 (Mar. 2020) 167–182, https://doi.org/10.1016/j.powtec.2020.01.056.
[54] E.L. Chan, K. Washino, Coarse grain model for DEM simulation of dense and dynamic particle flow with liquid bridge forces, Chem. Eng. Res. Des. 132 (2018) 1060–1069, https://doi.org/10.1016/j.cherd.2017.12.033.
[55] L. Lu, Y. Xu, T. Li, S. Benyahia, Assessment of different coarse graining strategies to simulate polydisperse gas-solids flow, Chem. Eng. Sci. 179 (2018) 53–63, https://doi.org/10.1016/j.ces.2018.01.003.
[56] S. Kanjilal, S. Schneiderbauer, A revised coarse-graining approach for simulation of highly poly-dispersegranular flows, Powder Technol. 385 (2021) 517–527.
[57] D. Queteschiner, T. Lichtenegger, S. Pirker, S. Schneiderbauer, Multi-level coarse-grain model of the DEM, Powder Technol. 338 (2018) 614–624, https://doi.org/10.1016/j.powtec.2018.07.033.
[58] M. Sakai, M. Abe, Y. Shigeto, S. Mizutani, H. Takahashi, A. Viré, J.R. Percival, J. Xiang, C.C. Pain, Verification and validation of a coarse grain model of the DEM in a bubbling fluidized bed, Chem. Eng. J. 244 (2014) 33–43, https://doi.org/10.1016/j.cej.2014.01.029.
[59] L. Lu, A. Morris, T. Li, S. Benyahia, Extension of a coarse grained particle method to simulate heat transfer in fluidized beds, Int. J. Heat Mass Transf. 111 (2017) 723–735, https://doi.org/10.1016/j.ijheatmasstransfer.2017.04.040.
[60] K. Chu, J. Chen, A. Yu, Applicability of a coarse-grained CFD–DEM model on dense medium cyclone, Miner. Eng. 90 (2016) 43–54, https://doi.org/10.1016/j.mineng.2016.01.020.
[61] S. Pietsch, P. Kieckhefen, S. Heinrich, M. Müller, M. Schönherr, F. Kleine Jäger, CFD-DEM modelling of circulation frequencies and residence times in a prismatic spouted bed, Chem. Eng. Res. Des. 132 (2018) 1105–1116, https://doi.org/10.1016/j.cherd.2018.01.013.
[62] S. Radl, B.C. Gonzales, C. Goniva, S. Pirker, State of the Art in Mapping Schemes for Dilute and Dense Euler-Lagrange Simulations, in: 10th International Conference on CFD In Oil & Gas, Metallurgical and Process Industries, 2014, pp. 103–112.
[63] Z.Y. Zhou, S.B. Kuang, K.W. Chu, A.B. Yu, Discrete particle simulation of particle-fluid flow: Model formulations and their applicability, J. Fluid Mech. 661 (2010) 482–510, https://doi.org/10.1017/S002211201000306X.
[64] T. Forgber, P. Toson, S. Madlmeir, H. Kureck, J.G. Khinast, D. Jajcevic, Extended validation and verification of XPS/AVL-Fire™, a computational CFD-DEM software platform, Powder Technol. 361 (2020) 880–893, https://doi.org/10.1016/J.POWTEC.2019.11.008.
[65] R. Beetstra, M.A. Van Der Hoef, J.A.M. Kuipers, Drag Force of Intermediate Reynolds Number Flow Past Mono- and Bidisperse Arrays of Spheres, AIChE J. 53 (2) (2007) 489–501, https://doi.org/10.1002/aic.
[66] S. Radl, C. Radeke, J.G. Khinast, S. Sundaresan, Parcel-based approach for the simulation of gas-particle flows, in: 8th Int. Conf. CFD Oil Gas, Metall. Process Ind., 2011, pp. 1–10.
[67] J. Kolář, P. Kovačík, T. Choděrová, Z. Grof, F. Štěpánek, Optimization of Wurster fluid bed coating: mathematical model validated against pharmaceutical production data, Powder Technol. 386 (2021) 505–518, https://doi.org/10.1016/j.powtec.2021.03.059.
[68] C. Rieck, A. Bück, E. Tsotsas, Estimation of the dominant size enlargement mechanism in spray fluidized bed processes, AIChE J. 66 (5) (2020) 1–18, https://doi.org/10.1002/aic.16920.
[69] D.J. Gunn, Transfer of heat or mass to particles in fixed and fluidised beds, Int. J. Heat Mass Transf. 21 (4) (1978) 467–476, https://doi.org/10.1016/0017-9310(78)90080-7.
[70] A. Asai, M. Shioya, S. Hirasawa, T. Okazaki, Impact of an Ink Drop on Paper, J. Imaging Sci. Technol. 37 (1993) 205–207, https://doi.org/10.1134/1.1333189.
[71] W.I.J. Kariuki, B. Freireich, R.M. Smith, M. Rhodes, K.P. Hapgood, Distribution nucleation: Quantifying liquid distribution on the particle surface using the dimensionless particle coating number, Chem. Eng. Sci. 92 (Apr. 2013) 134–145, https://doi.org/10.1016/j.ces.2013.01.010.
[72] C. Pei, H. Lin, D. Markl, Y.C. Shen, J.A. Zeitler, J.A. Elliott, A quantitative comparison of in-line coating thickness distributions obtained from a pharmaceutical tablet mixing process using discrete element method and terahertz pulsed imaging, Chem. Eng. Sci. 192 (2018) 34–45, https://doi.org/10.1016/j.ces.2018.06.045.
[73] R. Kolakaluri, Direct Numerical Simulations and Analytical Modeling of Granular Filtration, 2013.
[74] S. Radl, S. Sundaresan, A drag model for filtered Euler-Lagrange simulations of clustered gas-particle suspensions, Chem. Eng. Sci. 117 (2014) 416–425, https://doi.org/10.1016/j.ces.2014.07.011.
[75] M. Sakai, H. Takahashi, C.C. Pain, J. Latham, J. Xiang, Study on a large-scale discrete element model for fine particles in a fluidized bed, Adv. Powder Technol. 23 (5) (2012) 673–681, https://doi.org/10.1016/j.apt.2011.08.006.
[76] I.B. Celik, U. Ghia, P.J. Roache, C.J. Freitas, H. Coleman, P.E. Raad, Procedure for estimation and reporting of uncertainty due to discretization in CFD applications, J. Fluids Eng. Trans. ASME 130 (7) (2008) 0780011–780014, https://doi.org/10.1115/1.2960953.
[77] G.E. Mueller, Numerically packing spheres in cylinders, Powder Technol. 159 (2) (2005) 105–110, https://doi.org/10.1016/j.powtec.2005.06.002.
[78] W.T. Elam, A.R. Kerstein, J.J. Rehr, Critical properties of the void percolation problem for spheres, Phys. Rev. Lett. 52 (17) (1984) 1516–1519, https://doi.org/10.1103/PhysRevLett.52.1516.